








Continuous roller transfer-printing and automated metrology of >75,000 micro-LED pixels in a single shot

ELENI MARGARITI,^{*}  GEMMA QUINN, DIMITARS JEVTICS,^{*} 
BENOIT GUILHABERT,^{*}  MARTIN D. DAWSON,^{*}  AND MICHAEL J. STRAIN 

Institute of Photonics, Dept. of Physics, University of Strathclyde, Glasgow G1 1RD, UK

**eleni.margariti@strath.ac.uk*

Abstract: A continuous, single shot roller transfer printing process is presented for the large-scale hybrid integration of semiconductor devices. Transfer of a 320×240 pixel micro-LED array, representing >75,000 individual devices in a single shot with sub-micron relative position accuracy is demonstrated. The transfer printing process preserves the array geometry with pixel spatial location error less than 1 μm deviation from the as-designed layout. An automated sub-micron precision metrology system based on simple optical microscopy was developed to assess such large device populations and allow the assessment of yield.

Published by Optica Publishing Group under the terms of the [Creative Commons Attribution 4.0 License](#). Further distribution of this work must maintain attribution to the author(s) and the published article's title, journal citation, and DOI.

1. Introduction

Semiconductor micro-LEDs exhibit high optical contrast and brightness, high energy efficiency and long operating lifetimes, making them attractive options for display technologies across a range of scales [1]. Furthermore, due to their fast switching speeds [2] and compatibility with CMOS drive electronics, large arrays of micro-LED devices are rapidly maturing for display technology with applications in both research and industrial sectors including spatially modulated imaging [3], optical wireless communications [4], wearable/implantable optoelectronic displays [5], and biomedical sensor systems [6].

Advances in large area epitaxy of III-N materials-on-silicon are helping to address the issues of scaling micro-LED pixel array fabrication [7]. To deploy these micron scale devices in large format displays - e.g. TVs, smartphones, tablets, vehicle displays or flexible substrates (e.g. smart wristbands) [8] - parallel advances in mass transfer with high throughput and yield, compatible with manufacturing processes, are required. This large-scale device transfer requires the high yield integration of > 10's of thousands of individual pixels, ranging between 1-100 μm in size, onto non-native substrates with micrometer individual placement accuracy [9]. Moreover, this method should be compatible with back-end integration to drive electronics. Several techniques have been proposed in order to achieve this large-scale integration of micro-LED pixels onto non-native substrates including laser induced forward transfer [10] transfer printing [11] and flip chip bonding techniques [12] as it is not always possible to integrate devices through epitaxial growth-based methods [13].

Transfer printing is a particularly appealing methodology due to its compatibility with a wide range of material platforms [14,15], high integration accuracy device placement [16], and the potential for dense integration of devices from multiple material platforms on a single substrate [17]. Hybrid integration by transfer printing, especially in the field of displays, has seen rapid growth in recent years for both large and compact device sizes. There are a number of variations in the process for device transfer integration that have been demonstrated including laser-selective

release [18], electrostatic [19] or electromagnetic assisted pick-and-place [20], and polymer stamp-based pick-and-place. The last of these is the most common form of transfer printing and relies on the use of a viscoelastic material, commonly a PDMS stamp, in order to pick the device up from the donor substrate and transfer-print it to the receiver [21]. The process utilizes the relation between the adhesion energy of the PDMS and the material for deposition, bringing them into contact through van der Waals forces [22] or the use of surface adhesion layers [23]. Although a number of key demonstrations have been made using this technology, the ability to scale to manufacturing volumes remains an outstanding challenge.

To address this challenge, we have developed a roller-based transfer printing method which allows the printing of tens of thousands of devices in a single shot with high throughput. Roll transfer printing offers several advantages over other technologies, such as that it does not rely on remote force generation (magnetic, electrical or optical fields), and it does not require challenging environmental conditions. Moreover, it is a continuous process, without the need to disengage the roller, ensuring the simultaneous printing of numerous devices, making it highly efficient for large-scale production. A key benefit of using a roll-based process compared to standard planar pick-and-place transfer printing is its pseudo-1D contact area. Unlike the flat stamp that requires plane-to-plane alignment, which is difficult to scale on large areas, the roll stamp has a contact area that allows for a single axis alignment parallel to the roller axis. By shifting the one-dimensional contact region across the substrate, it becomes possible to process the entire substrate in a single continuous pass, thus facilitating future scale up this method [24]. Due to the large numbers of devices involved we also present an automated optical microscopy and image processing metrology system for assessing the process yield and accuracy in large device populations. We use the roller transfer printing method to fully integrate a micro-LED quarter Video Graphics Array (QVGA, 320×240 pixels) on a single polymer-coated silicon substrate. An automated roll-based transfer printing system is presented which allows the parallel printing of over 75,000 devices in one pass. Subsequently, the reliability and the accuracy of the roll-printing process is assessed with, a dynamic microscopy system, capturing local micrographs of the chip in step-and-save fashion to generate a large effective field of view (FOV) image [25]. The image is subsequently processed using an automated system to extract the position of the printed devices, the inter-device pitch values and the yield of the printing process. Analysis of a roller printed QVGA chip shows a transferred array accuracy of $430 \text{ nm} \pm 980 \text{ nm}$ with a total yield $>98\%$ ($>99.9\%$ excluding local donor chip related defects).

2. Continuous roller-printing system

Figure 1(a) shows a 3D schematic representation of the setup that was designed and constructed for this work. The single-shot roller printing technique was implemented using a custom setup based around a commercially available silicone roller with dimensions of 40 mm in diameter and 60 mm in axial length. The roller can be reused for multiple print cycles without performance degradation and cleaned by passing over adhesive pads. Although quantitative lifetime tests have not been carried out, a single roller has performed consistently over hundreds of cycles in our setup. A high vertical load translation stage allows for the control of the height of the roller with respect to the stage surface and, therefore, the subsequent applied pressure on the donor and receiver chips. Excessive load on roller tends to deform the surface from its nominal cylindrical shape [26,27] and so the system was operated at the limit of vertical load to enable a smooth rotation of the roller due to the stage translation. The roller itself is mounted on ball bearing hubs to minimize axial friction. The translation stage is an automated system with $2 \mu\text{m}$ on-axis accuracy, travel range of 150 mm and a maximum speed of 30 mm/s [Thorlabs' NRT150(M)]. The setup also incorporates two microscope cameras, one directly above the roller and one perpendicular to the leading edge of the roller, to observe the printing process. The donor and the receiver chips are fixed on the translation stage spaced by a few centimeters to

allow a one-roll printing process, as shown in Fig. 1. The design of donor and receiver chips are presented in section 3.

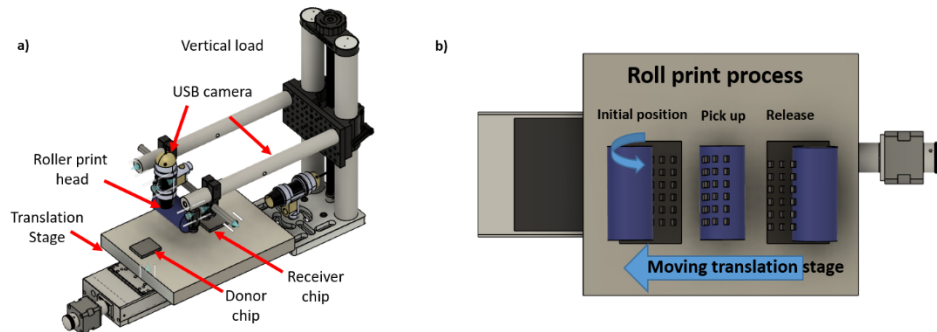


Fig. 1. (a) Schematic representation of the roll printing setup. (b) Printing process (left to right), devices are released from a donor onto the roller print head and then released onto a receiver chip.

The single-shot roller printing process is completed as follows: (1) the donor and receiver chips are placed on the translation stage with a separation equal to the circumference of the roller, (2) the roller surface is brought into contact with the translation stage with enough vertical load to produce rotational motion of the roller induced by translation of the stage surface, without any mechanical slip [28], (3) the translation stage moves with constant velocity so that first the donor chip passes under the roller and the devices are released from their suspended positions and adhere to the roller surface, (4) the roller makes a complete rotation driven by the translation stage until it makes contact with the receiver, (4) the devices on the roller surface make contact with the receiver chip and are transferred onto the surface from the roller. The entire roll-printing process takes 20 seconds, running with a translation stage velocity of 8 mm/s.

3. Membrane device design for high yield transfer printing

The mass transfer of LED pixels from their growth wafer to a host substrate requires these devices to be physically released from their native wafer. The growth of III-N optoelectronic devices on silicon substrates provides a convenient mechanism for the selective suspension of the epitaxial layers over the silicon substrate [29]. The suspended pixels presented in this work are fabricated using a III-N-on-Silicon material platform commonly employed for LED devices emitting at a wavelength of 450 nm. The fabrication process for producing suspended pixel devices is presented in [30]. In this work we limited fabrication to the mechanically suspended pixels in order to reduce the number of process steps required to produce samples for transfer. This enabled quicker turn-around of the multiple fabrication cycles required for iterative optimization of the transfer process. Active LED devices on this material would require additional steps to produce electronic contacts and insulation layers, but would not affect the mass transfer process that we focus on here. To produce the suspended pixels, a SiO₂ hard mask was deposited on the III-N material and spin coated with a positive tone photoresist. The suspended membrane pixel patterns were exposed in the photoresist mask using a direct-write laser lithography system, allowing for rapid prototyping of the various tether geometries discussed below. Nevertheless, the device geometries are compatible with standard photomask processing. The photoresist mask was then transferred into the silica hardmask using a CHF₃ reactive ion etch. The pattern was finally transferred into the semiconductor layers using an Ar₂:Cl₂ inductively coupled plasma reactive ion etch (ICP-RIE). The Si layer was anisotropically underetched using potassium hydroxide (KOH), resulting in voids in the Si material under the III-N pixels. The resulting suspended

membranes are supported by two anchors to surrounding support material that can be fractured during the pick-up process to release the membrane.

The shape, position and dimensions of the anchors were varied in III/V on Si test structures to assess compatibility with the roller printing process. Compared with standard planar pick-and-place transfer printing [13,14], the contact between the devices to be transferred and the pick-up head varies in two key aspects in the roller printing method. First, contact with the devices is not made across their full surface simultaneously, and the array is picked-up in a serial row by row manner. Second, the curved surface of the roller and the directionality of the contact progression can induce torsion of the membranes. These effects are also dependent on the membrane size and roller radius of curvature (ROC). Large ROC rollers and smaller membranes will be less likely to be affected by torsional effects as the surface to surface contact becomes more uniform during the printing process. To study the mechanical effects of the anchor geometries on the printing yield, test membranes of $100 \times 100 \mu\text{m}^2$ dimensions were fabricated incorporating variations in tether shape and relative position to the membrane structure. Three main anchor geometries were trialed; rectangular, tapered and bow tie shaped, as shown in Fig. 2. The different shapes correspond to different breaking points during pick up process. The study of these shapes includes critical dimensions in the range between 2-10 μm . For repeatable tether cleaving and membrane stability, the anchor dimensions were found to be: i) $10 \times 5 \mu\text{m}^2$ for rectangular shape, ii) 7 μm long and 10 - 5 μm in width for the tapered geometry and iii) 10 μm long, 4 μm major dimension width and 2 μm minimum width for the bow-tie shaped anchors. Figure 2 shows scanning electron microscopy (SEM) images of the selected anchor designs in after suspension on their native silicon substrate. Each of these designs performed equally well in printing trials.

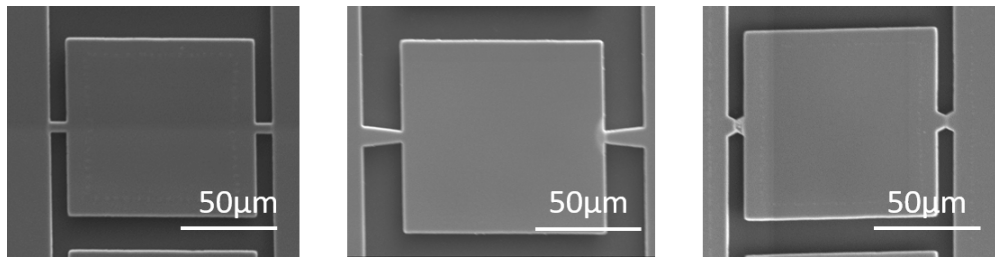


Fig. 2. Plan view of SEM images of three pixel anchor designs, from left to right: rectangular, triangular, bow-tie.

In addition to tether geometry, the placement of the tether supports relative to the membrane layout was investigated. For planar transfer printing processes, tethers arranged asymmetrically around the membrane's central axis are often employed [22,31]. The roller printing method requires a different approach due to the torsional effects noted above. If asymmetrical tether positions are used, then rotation of the membrane around an axis normal to its center of surface area can be induced, as the roller surface to membrane contact is non-uniform and varying during the pick-up and release processes. This rotation is also dependent on the direction of travel of the roller with respect to the tethers as shown in Fig. 3(a). Figure 3(b) shows examples of failed membrane pick-up due to these rotational effects, where devices can fail to release, collapse onto the substrate, or even slide under the mechanical support structures surrounding the pick-up area, depending on the direction of roller travel.

For smaller pixel dimensions, a single tether geometry can be employed. For the demonstration of single shot roller printing, membrane pixels with dimensions of $30 \times 30 \mu\text{m}^2$ and a center-to-center pitch of 50 μm were fabricated (549 dpi). Figure 4. shows an optical microscope image of a single pixel from the array, with a single tether point located at the mid-point of one edge of the

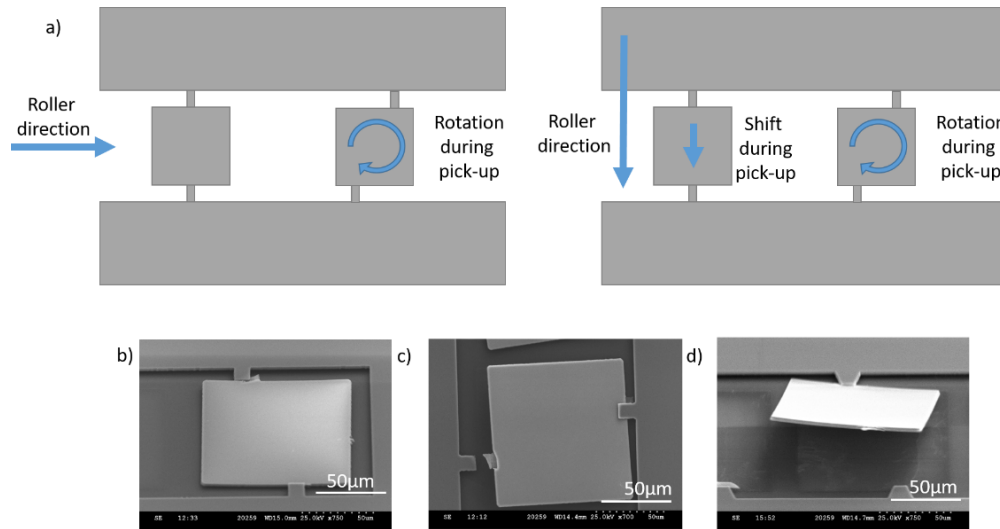


Fig. 3. a) Plan view schematic of the various effects during membrane pick-up dependent on the anchor location geometry and roller translation direction. SEM images of examples of (b) collapsed membrane (c) shifted membrane trapped by anchor support, and (d) rotated and partially released membrane.

pixel. An array of 320 x240 such pixels was used, corresponding to a quarter video graphics array (QVGA) with a total of 76,800 individual pixels. The silicon receiver chips were coated with a thin adhesive layer of fast-cured adhesive optical polymer (Norland NOA 85) to aid device release from the roller transfer head.

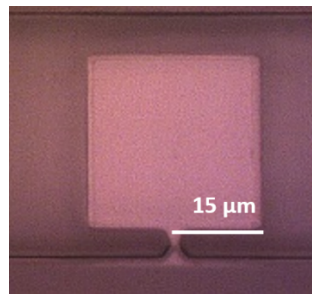


Fig. 4. Plan view optical microscope image of a single pixel from the QVGA array, as fabricated on the donor chip with a single tether point.

4. Roller print head surface roughness

For large scale, high yield transfer, the surface properties of the roller transfer head are crucial. Silicone rollers are widely available for applications in surface cleaning and we compare three of these as a function of surface roughness. It has been shown previously that non-uniformity in roller printing can occur due to the deviations in the cylindrical profile of the roller [32]. Operating the roller under some applied pressure may mitigate longer-range non-uniformities but local surface roughness remains an issue. We trialed the printing process with nominally identical donor and receiver chips using 3 different rollers with low, medium and high surface roughness respectively. We characterized the surface roughness of each silicone roller by excising a small

portion of material and imaging it using an atomic force microscope (AFM), as shown in Fig. 5. The large scale peak to peak surface roughness for the 3 rollers was found to be on the order of 18, 1.4 and 0.3 μm respectively. The final column in Fig. 5 shows the result of test printing of pixel arrays with each roller. We have found that for the rollers with higher roughness values, device transfer does occur but with significant loss of devices and positional shifts from the uniform array. By contrast, the 0.3 μm roughness roller demonstrates faithful device transfer with good yield and minimal spatial deviations from the as-fabricated uniform array grid arrangement. Therefore, for the demonstration of the full 320×240 pixel array transfer, the 0.3 μm surface roughness roller was selected.

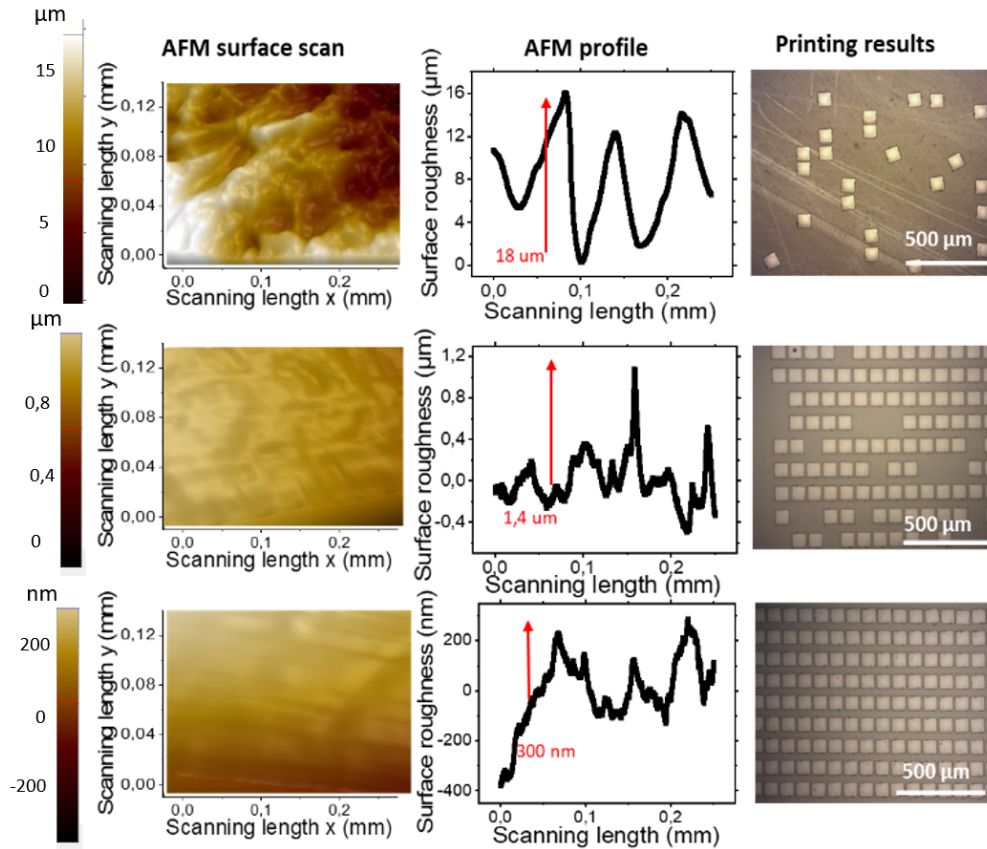


Fig. 5. Illustration of the effects of roller surface roughness on transfer printing process. Left hand side and center columns show AFM surface and profile scans respectively for three roller print heads with different surface roughness. The red arrow on AFM profiles indicates the 'peak-to-peak' values. The right hand side column shows optical microscope images of the roller transfer printing results from nominally identical donor chips using the respective rollers.

5. Automated metrology system

Assessing the yield of the transfer process and any distortion of the as-fabricated spatial pixel arrangement for $>75,000$ devices requires an automated process. Here we developed hardware and software for the automated analysis of these large arrays of membranes. Optical microscope images of the samples were captured using a commercial optical microscope with a nanometric

accuracy translation stage mounted as the sample holder. Automated scanning measurements were captured and stitched together with high precision to form large effective field of view images with resolution limited by the optical system. Two imaging setups were employed in this work, based on image capture times. Imaging with a 50X magnification objective lens provides an imaging resolution down to 94 nm/pixel using the silicon camera mounted on our system. However, as total processing time increases with the number of sub-images required, we used a 10X magnification objective lens, corresponding to a resolution of to 452 nm/pixel, for assessment of the full 320×240 device arrays. The automated system was designed to characterize the yield of the transfer process (i.e. assessment of missing membrane devices in a printed array) and the relative positional accuracy of the print (i.e. the device to device pitch as compared with the as-fabricated array) [25]. Figure 6 shows a schematic overview of the assessment process, highlighting the measurement parameters of lateral pitch error in x and y dimensions, rotational error and missing device identification.

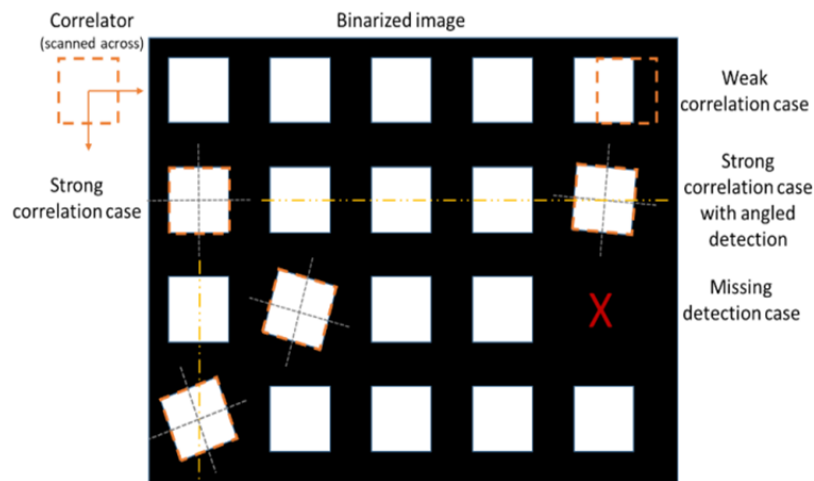


Fig. 6. Schematic of the cross-correlation based metrology process. The image shows a binarized form of the optical microscope image, where the dotted square represents the ideal pixel form used to perform the cross-correlation assessment in x, y and θ_z dimensions. Examples of recognized device positions and missing device cases are shown.

The image analysis was implemented in Matlab and makes use of standard tools in the image processing toolbox. First, each optical microscope image is converted to a binary format, followed by an edge detection process to obtain the mechanical edges of the membrane devices. The threshold for the binarization is adapted and defined automatically according to the dynamic range of the raw image. The image was excised of small objects and spatial defects using a ‘morphological opening’ tool that performs a shape and scale-based thresholding operation. An object recognition tool was then employed to identify approximately square objects in the image. A kernel convolution matrix was used for edge detection of each identified device within the image. The object center points were extracted using a cross-correlation operation with an idealized prototype of the membrane wire-model within the range of $\pm 50 \mu\text{m}$ across the point of interest, similar to that presented in [33]. The peak of the local cross-correlation corresponds to the extracted device center point within the camera pixel resolution. An example of such a cross-correlation measurement is shown in Fig. 7(a)). The angular rotation of the object is calculated in a similar fashion where the cross-correlation is calculated as a function of the relative rotation of the prototype object within the range of ± 10 degrees of rotation. Figure 7(b)) shows calculated cross-correlation curves as a function of angle, the maximum of the central peaks

corresponds to the extracted device rotation angle. Finally, in cases where the cross-correlation maxima fall below a threshold value, the system assesses this as a missing device.

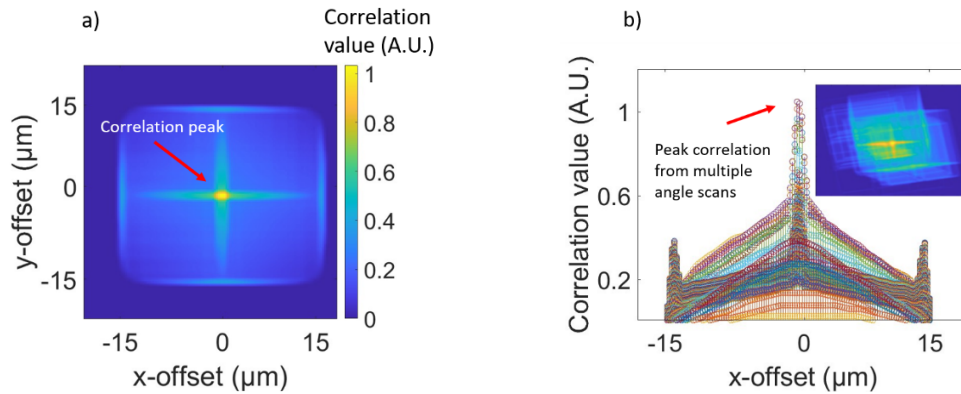


Fig. 7. a) Cross-correlation scan result of a pixel in x and y dimensions. The central bright spot represents the extracted object center point. b) Cross-correlation scans as a function of angular rotation and lateral offset in one dimension. The absolute peak in the family of curves represents the best angular fit to the pixel under consideration. (Inset: 2D map of angular correlation scans with bright central point showing pixel center).

The metrology system compiles a list of spatial positions corresponding to each recognized device and their local rotation, and the total number of missing devices. Yield is simply calculated from the missing device numbers, and can be calculated for sub-sections of the full array using the extracted local spatial coordinates. The measured pitch values between each device and its 4 adjacent neighbors are calculated using a loop which corrects for any missing devices. The final results of the analysis are used to produce statistical distributions of center-to-center pitch values, rotation angles and number of missing pixels, all of which can be assessed over local or global areas.

6. Analysis of pre- and post-printing QVGA pixel arrays

The automated analysis method was first assessed using an as-fabricated reference sample consisting of a QVGA format pixel donor chip. The extracted geometry results were then directly compared with the targeted square array pitch of the devices defined by the photolithography mask design. Figure 8 shows the initial image of the QVGA patterned devices on a Si substrate at three different magnifications.

To assess the limits of the method, the highest magnification objective in our microscopy system was selected for this analysis, namely a 50X infinity corrected lens corresponding to a pixel resolution of 94 nm/pixel at the camera image plane. To limit scanning time of the microscopy system a sub-section of the array, comprising 900 devices was used for this analysis. The histogram of extracted pitch value errors is shown in Fig. 9. The pitch error is defined here as the deviation of the extracted pitch value, between neighboring devices, from the as-designed value. Since the device pitch in both x and y directions is identical, the pitch between nearest neighbors in both x and y dimensions are reported in a single dataset. For this set of measured devices, the extracted pitch error has a mean value of 120 nm and a standard deviation of 830 nm. The mean value is close to the pixel resolution of the imaging system, while the standard deviation is nearly an order of magnitude larger than the pixel resolution. The device positional accuracy should be limited only by the lithographic accuracy of the fabrication and so the standard deviation of 830 nm can be taken as a lower limit of the accuracy of the measurement technique. No

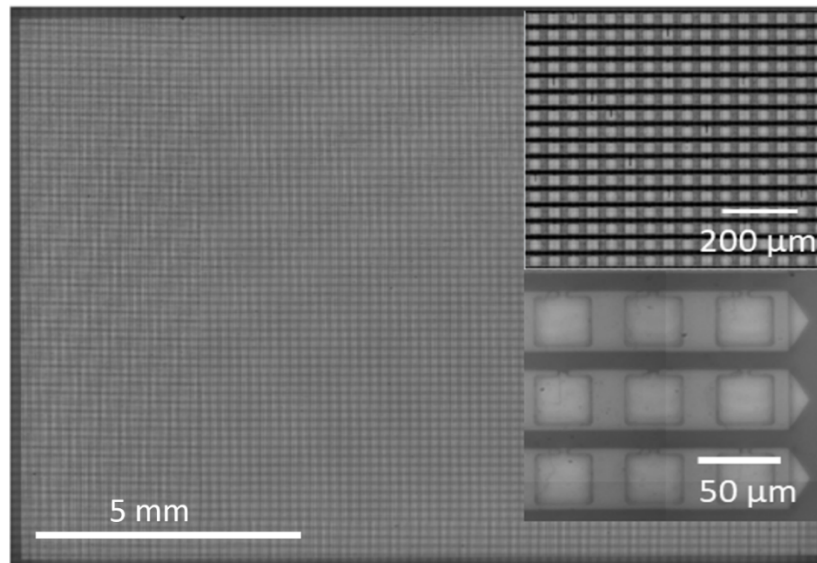


Fig. 8. Scanning optical microscopy image of an as-fabricated pixel array with 50 μm pitch in both x and y directions. (Insets show the same device at increasing magnification levels).

measurable rotation of devices from their nominally ideal position was detected to within the 1° resolution of the automated scan.

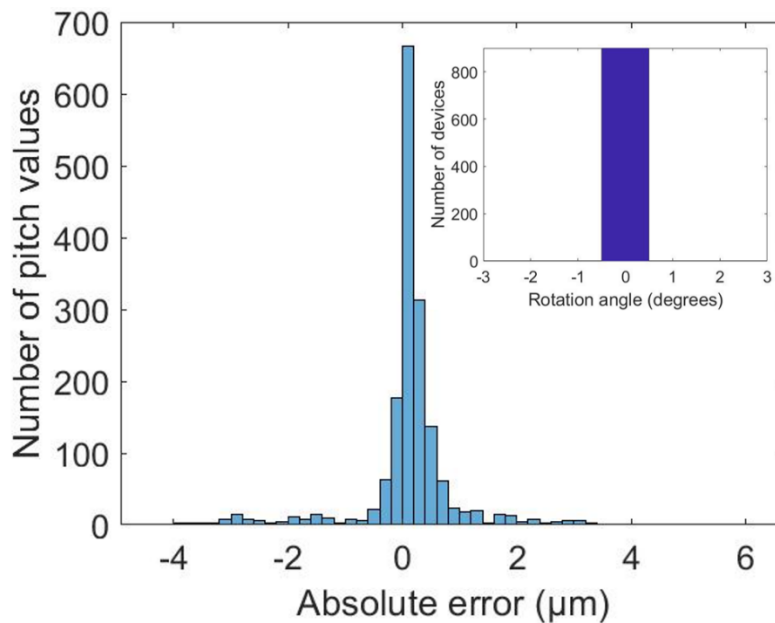


Fig. 9. Extracted histogram in both x and y directions of the relative pitch error in the as-fabricated pixel array donor chip (Inset: histogram of the extracted pixel rotation error).

To validate the yield assessment a test print was carried out using a donor chip with a deliberately large fraction of defects, resulting in a low yield print result. Figure 10 shows a part of the processed microscopy image. The vacant grid sites are clearly visible in the processed

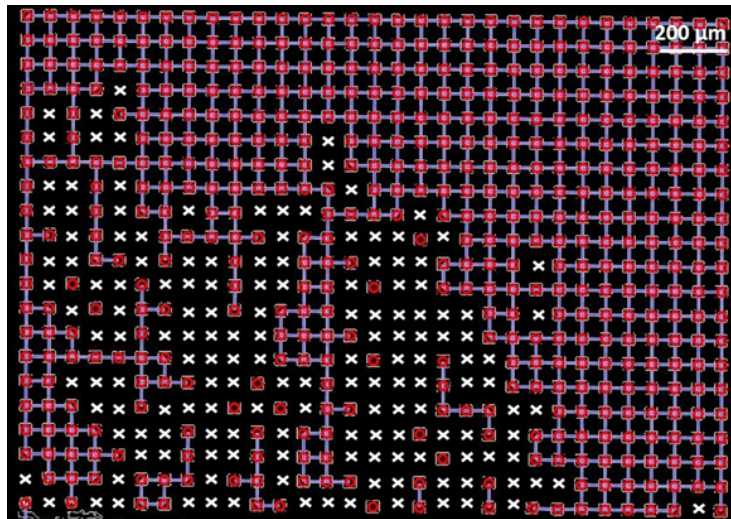


Fig. 10. Automated metrology tool output showing identified device locations (red circles), nearest neighbor device pitches (blue lines) and missing device locations (white crosses).

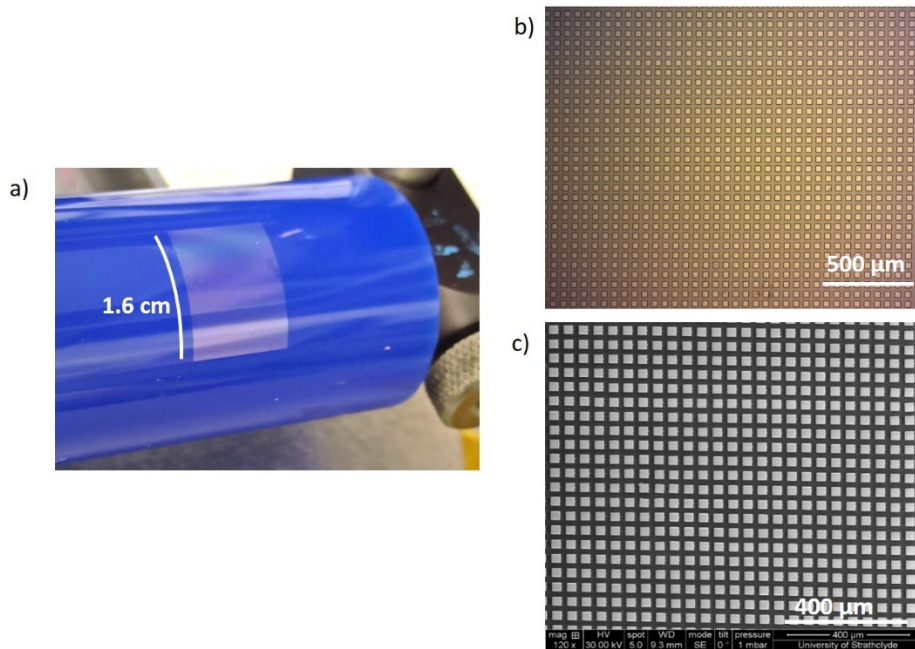


Fig. 11. a) Image of the roller print head mid-way through the process with the QVGA pixel array visible on the surface. b) Optical microscope and c) SEM images of sub-sections of the transfer printed pixel array.

image and are marked with an 'x' at the expected location of the pixel center. The extracted pixel pitch values (blue lines) are only defined between nearest neighbor pixels and, as designed, eliminate distances covering missing device elements. The extracted center positions for the successfully transferred pixels are shown as red circles in the image.

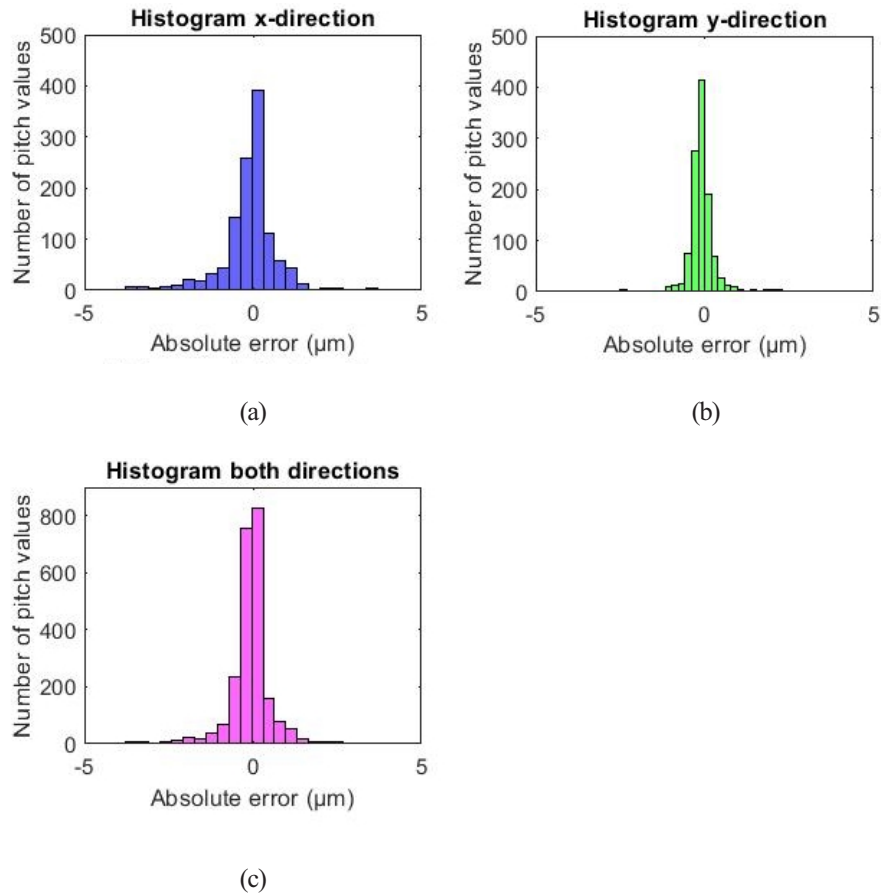


Fig. 12. Extracted histograms of the relative pitch error in a sub-section of the printed pixel array receiver chip, using a 50X optical microscope objective. Histograms for (a) x and (b) y directions are presented individually and (c) as a combined data set.

The continuous roll printing process was then carried out on a full QVGA pixel array. Figure 11(a) shows the pixel array after pick-up by the roller print head, during the continuous roller transfer stage. Figure 11(b) and (c) respectively show optical microscope and SEM images of a sub-section of the printed array.

A sub-section of the full printed array was imaged using the 50X objective scanning optical microscopy system, and processed with the automated metrology system. As before, the pixel pitch values are reported as an error value from the designed value of $50\ \mu\text{m}$ in both x and y dimensions, as shown in Fig. 12(a) and 12(b)). This high resolution sub array produced mean offset and standard deviation values of 120 and 730 nm, respectively, for the full dataset. As these values are of the same order of magnitude as the measured values from the as-fabricated device we can be confident they represent the effects of the printing process and are not measurement limited.

The scanning microscopy was then carried out over the full array using a 10X magnification objective lens to reduce throughput time. The 10X objective setup has a spatial resolution of 720 nm/pixel at the image plane. The full QVGA area of $12 \times 15\ \text{mm}^2$ takes 160 minutes with the 10X objective and 1800 minutes with the 50X objective. The scanning time of the system is limited by the current implementation of the electronic interfacing between the camera, stage

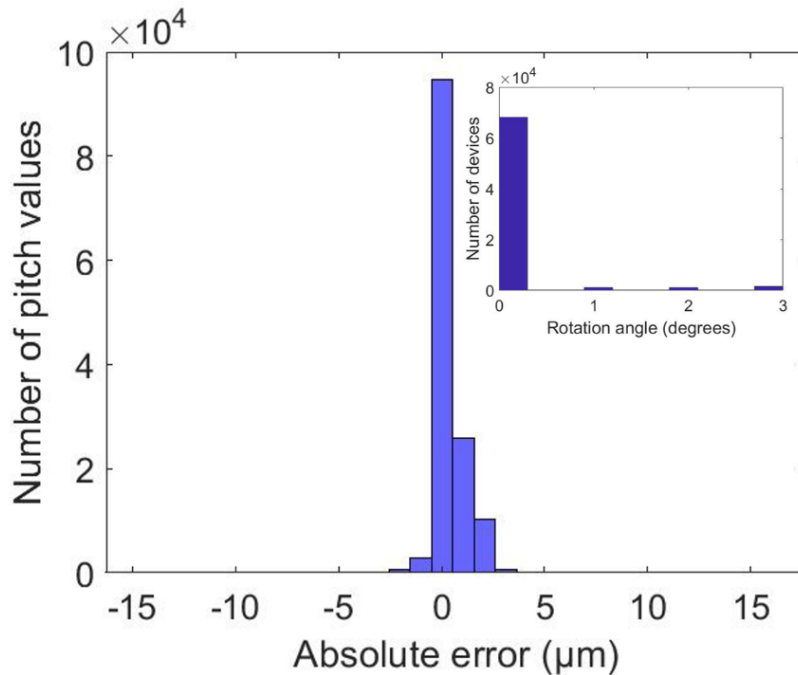


Fig. 13. Histogram of pitch offset error for the full roller transfer printed QVGA pixel array (Inset: histogram of the rotation).

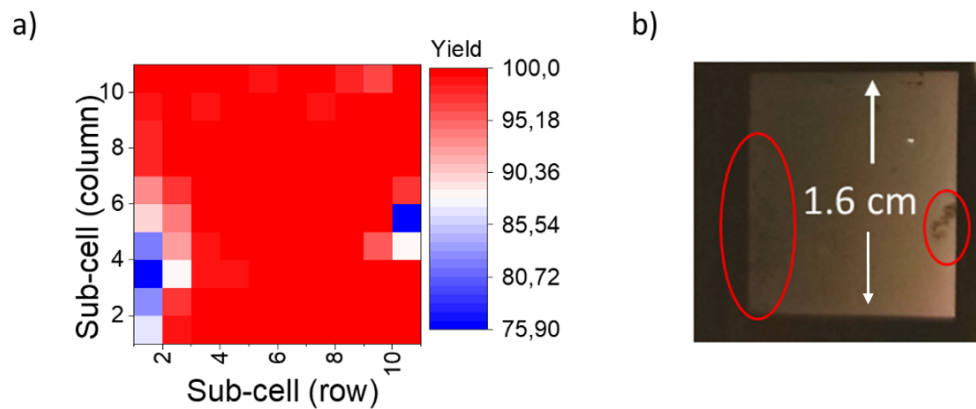


Fig. 14. a) Local area process yield map. b) Photograph of the printed device array, highlighting areas of local yield issues corresponding to (a).

controller and computer. By optimizing the data connection rates and removing communications latencies the scan time could be improved by around two orders of magnitude. Figure 13. shows the histogram of extracted pitch error across both x and y dimensions. The mean pixel pitch error is 430 nm, with a standard deviation of 980 nm. These figures are comparable with the high-resolution sub-section measurements. The distribution of pitch error across the array as a function of spatial location was assessed and did not demonstrate any local trends, giving confidence in the uniformity of the process over relatively large areas. The analysis of pixel rotation showed negligible rotation effects to within the 1° accuracy of the method.

The absolute yield of the array printing process was 98%, however, the defects were spatially localized within two small areas with yields of ~80%. As mentioned previously, a significant advantage of our method is that the position, rotation and yield results are associated with coordinate locations in the grid, allowing for spatially resolved analysis of the results. Figure 14(a) shows a heat map of the calculated transfer yield for the whole chip divided into 10×10 local sub-areas, each of these representing 32×24 devices in column and row, respectively, on a color scale. Two clear areas of low process yield are apparent in this analysis, while the majority of the chip approaches unity yield. Figure 14(b) shows a large FOV image of the printed array where the local, low yield areas of the array are obvious, highlighted by the red bounding ellipses. The donor chip for this process was re-assessed using optical microscopy after the printing stage to correlate defects in the printed array with the remaining donor pixel sites. The areas of low yield on the receiver corresponded to areas on the donor where the pixels had not been released and were still in-place. Inspection showed that these pixels were not fully-fabricated as membranes, potentially due to their proximity to the chip edges causing issues with a lithography step. Attempts to print these membranes using a standard planar single device transfer printing method [34] were unsuccessful highlighting the failure of membrane release. The areas of lower yield are therefore attributed to donor processing issues, rather than the printing process itself.

7. Conclusions

In this work, we presented an automated roll-transfer printing method that allows the printing of tens of thousands of devices in a single continuous process. We illustrated the capability of the system for printing micro-LED arrays. In order to evaluate our method in terms of positional accuracy, rotation and yield, we developed an automated sub-micron inspection method that we used both for the analysis of an as-fabricated donor chip and the resultant roll printed array. The as-fabricated chip analysis showed a measurement limited performance, with a standard deviation of the pixel pitch error of 830 nm. The fully transferred array of >75,000 devices presented a mean pitch error of 430 nm and a standard deviation of 980 nm. The full array yield of 98% was shown to be spatially dependent with the majority of the chip area yield >99.9% and defects dominated by small areas where the donor chip processing had failed. This work shows the potential for hybrid materials device integration at scale, compatible with the well-established infrastructure and semiconductor processes developed in industrial foundry manufacturing.

Funding. Fraunhofer UK; Royal Academy of Engineering; Innovate UK (50414); Engineering and Physical Sciences Research Council (EP/M013243/1, EP/P013597/1, EP/R03480X/1, EP/V004859/1).

Acknowledgments. We gratefully acknowledge Sheila Hamilton of Teknek (Inchinnan, UK) for provision of sample rollers which helped to initiate the investigations. We would also like to thank Dr. Navid Bani Hassan for providing useful knowledge in programming.

Disclosures. The authors declare no conflicts of interest.

Data availability. Data underlying the results presented in this paper are available in [35].

References

1. Z. Chen, S. Yan, and C. Danesh, "MicroLED technologies and applications: characteristics, fabrication, progress, and challenges," *J. Phys. D: Appl. Phys.* **54**(12), 123001 (2021).
2. K. S. Yeo, W. X. Ng, M. Y. Soh, and T. H. Teo, "Micro-LED arrays for display and communication: Device structure and driver architecture," in *Proceedings of International Conference on ASIC*, Jul. 2017, 2017-October, pp. 993–996, doi: 10.1109/ASICON.2017.8252645.
3. E. Salvador-Balaguer, P. Latorre-Carmona, C. Chabert, F. Pla, J. Lancis, and E. Tajahuerce, "Low-cost single-pixel 3D imaging by using an LED array," *Opt. Express* **26**(12), 15623 (2018).
4. D. M. Maclure, J. J. D. McKendry, M. S. Islam, E. Xie, C. Chen, X. Sun, X. Liang, X. Huang, H. Abumarshoud, J. Herrnsdorf, E. Gu, Harald Haas, and M. D. Dawson, "10 Gbps wavelength division multiplexing using UV-A, UV-B, and UV-C micro-LEDs," *Photonics Res.* **10**(2), 516 (2022).
5. H. E. Lee, Daewon Lee, T.-I. Lee, J. H. Shin, G.-M. Choi, C. Kim, S. H. Lee, J. H. Lee, Y. H. Kim, S.-M. Kang, S. H. Park, I.-S. Kang, T.-S. Kim, B.-S. Bae, and J. L. Keon, "Wireless powered wearable micro light-emitting diodes," *Nano Energy* **55**, 454–462 (2019).

6. J. J. D. McKendry, E. Gu, N. McAlinden, N. Laurand, K. Mathieson, and M. D. Dawson, "Micro-LEDs for biomedical applications," *Semicond. Semimetals* **106**, 57–94 (2021).
7. C. J. Chen, H. C. Chen, J. H. Liao, C. J. Yu, and M. C. Wu, "Fabrication and characterization of active-matrix 960×540 Blue GaN-Based Micro-LED Display," *IEEE J. Quantum Electron.* **55**(6), 1–6 (2019).
8. R. S. Cok, M. Meitl, R. Rotzoll, G. Melnik, A. Fecioru, A. J. Trindade, B. Raymond, S. Bonafede, D. Gomez, T. Moore, C. Prevatte, E. Radauscher, S. Goodwin, P. Hines, and C. A. Bower, "Inorganic light-emitting diode displays using micro-transfer printing," *J. Soc. Inf. Disp.* **25**(10), 589–609 (2017).
9. A. Paranjpe, J. Montgomery, S. M. Lee, and C. Morath, "45-2: Invited Paper: Micro-LED Displays: Key Manufacturing Challenges and Solutions," *SID Symp. Dig. Tech. Pap.* **49**(1), 597–600 (2018).
10. R. Miller, V. Marinov, O. Swenson, Z. Chen, and M. Semler, "Noncontact selective laser-assisted placement of thinned semiconductor dice," *IEEE Trans. Compon., Packag. Manuf. Technol.* **2**(6), 971–978 (2012).
11. C. A. Bower, M. A. Meitl, B. Raymond, E. Radauscher, R. Cok, S. Bonafede, D. Gomez, T. Moore, C. Prevatte, B. Fisher, R. Rotzoll, G. A. Melnik, A. Fecioru, and A. J. Trindade, "Emissive displays with transfer-printed assemblies of $8\mu\text{m} \times 15\mu\text{m}$ inorganic light-emitting diodes," *Photonics Res.* **5**(2), A23 (2017).
12. P. Li, X. Zhang, L. Qi, and K. M. Lau, "Full-color micro-display by heterogeneous integration of InGaN blue/green dual-wavelength and AlGaInP red LEDs," *Opt. Express* **30**(13), 23499 (2022).
13. X. Zhou, P. Tian, C.-W. Sher, J. Wu, H. Liu, R. Liu, and H.-C. Kuo, "Growth, transfer printing and colour conversion techniques towards full-colour micro-LED display," *Prog. Quantum Electron.* **71**, 100263 (2020).
14. B. Corbett, R. Loi, W. Zhou, D. Liu, and Z. Ma, "Transfer print techniques for heterogeneous integration of photonic components," *Prog. Quantum Electron.* **52**(xxxx), 1–17 (2017).
15. J. Yoon, S. M. Lee, D. Kang, M. A. Meitl, C. A. Bower, and J. A. Rogers, "Heterogeneously integrated optoelectronic devices enabled by micro-transfer printing," *Adv. Opt. Mater.* **3**(10), 1313–1335 (2015).
16. J. McPhillimy, B. Guilhabert, C. Klitis, M. D. Dawson, M. Sorel, and M. J. Strain, "High accuracy transfer printing of single-mode membrane silicon photonic devices," *Opt. Express* **26**(13), 16679 (2018).
17. D. Jevtics, J. A. Smith, John McPhillimy, B. Guilhabert, P. Hill, C. Klitis, A. Hurtado, M. Sorel, H. H. Tan, C. Jagadish, M. D. Dawson, and M. J. Strain, "Spatially dense integration of micron-scale devices from multiple materials on a single chip via transfer-printing," *Opt. Mater. Express* **11**(10), 3567 (2021).
18. R. Saeidpourazar, M. D. Sangid, J. A. Rogers, and P. M. Ferreira, "A prototype printer for laser driven micro-transfer printing," *J. Manuf. Process.* **14**(4), 416–424 (2012).
19. J. A. Higginson and S. Clara, "Method of transferring and bonding an array of micro devices," Patent WO2013119671A1 (2013).
20. Q. Yu, A. Li, X. Yu, H. Zhou, and H. Cheng, "Design of the magnetic stamp film for electromagnetic- assisted transfer printing," *J. Appl. Mech.* **88**(7), 1–8 (2021).
21. C. A. Bower, M. Meitl, S. Bonafede, and D. Kneeburg, "Micro-transfer-printing : deterministic assembly of microscale components using elastomer stamps," *IEEE Sensors*, pp. 2111–2113, 2014.
22. J. McPhillimy, C. Klitis, P. Hill, S. May, B. Guilhabert, M. D. Dawson, M. Sorel, and M. J. Strain, "Towards 3D optical integration by micro-transfer printing of ultra-thin membrane devices," *2018 Br. Irish Conf. Opt. Photonics, BICOP 2018 - Proc.*, no. December, pp. 1–4, 2019, doi: 10.1109/BICOP.2018.8658325.
23. C. Wang, C. Linghu, S. Nie, C. Li, Q. Lei, X. Tao, Y. Zeng, Y. Du, S. Zhang, K. Yu, H. Jin, W. Chen, and J. Song, "Programmable and scalable transfer printing with high reliability and efficiency for flexible inorganic electronics," *Sci. Adv.* **6**(25), eabb2393 (2020).
24. B. K. Sharma, B. Jang, J. E. Lee, S.-H. Bae, T. W. Kim, H.-J. Lee, J.-H. Kim, and J.-H. Ahn, "Load-controlled roll transfer of oxide transistors for stretchable electronics," *Adv. Funct. Mater.* **23**(16), 2024–2032 (2013).
25. E. Margariti, B. Guilhabert, D. Jevtics, M. D. Dawson, and M. J. Strain, "Sub-micron-accuracy automated position and rotation registration method for transferred devices," *2021 IEEE Photonics Conf. IPC 2021 - Proc.*, pp. 2021–2022, 2021, doi: 10.1109/IPC48725.2021.9592935.
26. P. B. Lindley, "Load-compression relationships of rubber units," *J. Strain Anal.* **1**(3), 190–195 (1966).
27. A. Aschenbrenner, B. Schleich, S. Tremmel, and S. Wartzack, "A variational simulation framework for the analysis of load distribution and radial displacement of cylindrical roller bearings," *Mech. Mach. Theory* **147**, 103769 (2020).
28. A. V. Borisov, I. S. Mamaev, and I. A. Bizyaev, "The hierarchy of dynamics of a rigid body rolling without slipping and spinning on a plane and a sphere," *Regul. Chaotic Dyn.* **18**(3), 277–328 (2013).
29. C. A. Bower, E. Menard, S. Bonafede, and S. Burroughs, "Transfer-printed microscale integrated circuits," in *Proceedings - Electronic Components and Technology Conference*, 2009, pp. 618–623, doi: 10.1109/ECTC.2009.5074077.
30. A. J. Trindade, B. Guilhabert, D. Massoubre, D. Zhu, N. Laurand, E. Gu, I. M. Watson, C. J. Humphreys, and M. D. Dawson, "Nanoscale-accuracy transfer printing of ultra-thin AlInGaIn light-emitting diodes onto mechanically flexible substrates," *Appl. Phys. Lett.* **103**(25), 253302 (2013).
31. K. Buehler, G. Lorenz, M. Mittag, U. Krieger, N. Heise, S. Wicht, and R. Gerbach, *Falk Naumann IEEE Electronics Packaging Society, Institute of Electrical and Electronics Engineers, and M. and M.-P. S. and E. in M. and M. (EuroSimE 20th International Conference on Thermal, "Micro-Transfer-Printing and Potential Process Optimizations by FEA,"* 2019, pp. 1–8.
32. Y. Kusaka and N. Fukuda, "Decomposition of pattern distortions by the Spread polynomial model in roll-to-sheet reverse offset printing," *J. Micromech. Microeng.* **30**(9), 095007 (2020).

33. J. McPhillimy, D. Jevtics, B. J. E. Guilhabert, C. Klitis, A. Hurtado, M. Soel, M. D. Dawson, and M. J. Strain, "Automated nanoscale absolute accuracy alignment system for transfer printing," *ACS Appl. Nano Mater.* **3**(10), 10326–10332 (2020).
34. B. Guilhabert, J. McPhillimy, S. May, C. Klitis, M. D. Dawson, M. Sorel, and M. J. Strain, "Hybrid integration of an evanescently coupled AlGaAs microdisk resonator with a silicon waveguide by nanoscale-accuracy transfer printing," *Opt. Lett.* **43**(20), 4883 (2018).
35. E. Margariti, G. Quinn, D. Jevtics, B. Guilhabert, M. D. Dawson, and M. J. Strain, "Continuous roller transfer-printing and automated metrology of >75,000 micro-LED pixels in a single shot: data," University of Strathclyde, 2023, <https://doi.org/10.15129/a2056265-495a-422a-b65f-0570923e471a>.